Title
Interfacial Effects in ε-LixVOPO4 and Evolution of the Electronic Structure

Permalink
https://escholarship.org/uc/item/4dt9c5zn

Journal
Chemistry of Materials, 27(24)

ISSN
0897-4756

Authors
Quackenbush, NF
Wangoh, L
Scanlon, DO
et al.

Publication Date
2015-12-22

DOI
10.1021/acs.chemmater.5b02145

Peer reviewed

CHEMISTRY OF MATERIALS

Article

pubs.acs.org/cm

Interfacial Effects in ε-Li_xVOPO_4 and Evolution of the Electronic Structure

N. F. Quackenbush,[†] L. Wangoh,[†] D. O. Scanlon,[‡,§] R. Zhang,[†] Y. Chung,[∥] Z. Chen,[⊥,∥] B. Wen,[#] Y. Lin,[∇] J. C. Woicik,[○] N. A. Chernova,[∥] S. P. Ong,[∇] M.S. Whittingham,[∥] and L. F. J. Piper*[,†,◆]

[†]Department of Physics, Applied Physics and Astronomy, Binghamton University, Binghamton, New York 13902, United States

[‡]University College London, Kathleen Lonsdale Materials Chemistry, Department of Chemistry, 20 Gordon Street, London WC1H 0AJ, United Kingdom

[§]Diamond Light Source Ltd., Diamond House, Harwell Science and Innovation Campus, Didcot, Oxfordshire OX11 0DE, United Kingdom

[∥]The Northeast Center for Chemical Energy Storage (NECCES), State University of New York at Binghamton, Binghamton, New York 13902, United States

[⊥]College of Chemistry & Chemical Engineering, Central South University, Changsha 410083, China

[#]Chemistry and Materials, State University of New York at Binghamton, Binghamton, New York 13902, United States

[∇]Department of NanoEngineering, University of California, San Diego, 9500 Gilman Drive, Mail Code 0448, La Jolla, California 92093, United States

[○]Materials Science and Engineering Laboratory, National Institute of Standards and Technology, Gaithersburg, Maryland 20899, United States

[◆]Materials Science & Engineering, Binghamton University, Binghamton, New York 13902, United States

Supporting Information

ABSTRACT: The epsilon polymorph of vanadyl phosphate ε-$VOPO_4$ is a promising cathode material for high-capacity Li ion batteries, owing to its demonstrated ability to reversibly incorporate two lithium ions per redox center. As lithium is inserted into the nanosized particles within the cathode, the electrochemical reaction can be largely affected by the interfacial chemistry at the nanoparticle surface. We performed X-ray photoelectron spectroscopy using both soft (XPS) and hard (HAXPES) X-rays to chemically distinguish and depth-resolve the interfacial phase transitions in ε-$VOPO_4$ electrodes as a function of electrochemical discharge. Our analysis shows that the second lithium reaction begins before the full incorporation of the first lithium. This results in a pronounced lithium gradient within the nanoparticles, with the ε-Li_2VOPO_4 phase only forming near the surface. These results indicate that a disruption of the kinetics are limiting the realized capacity in our hydrothermally synthesized ε-$VOPO_4$. Moreover, from inspection of the valence band region, we were able to monitor the evolution of ε-$VOPO_4$ to ε-Li_2VOPO_4 at the surface of our nanoparticles. These assignments are confirmed by hybrid density functional theory of the three end phases.

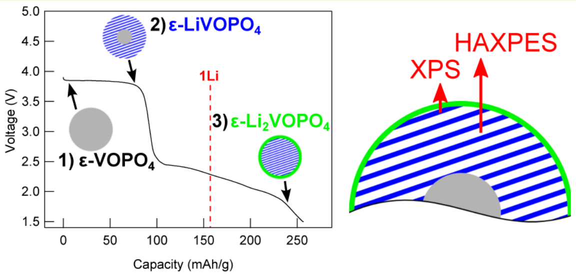

INTRODUCTION

Chemical energy storage in the form of rechargeable Li ion batteries will play an essential role in the future of our energy landscape.[1,2] The development of high energy Li ion batteries depends largely on the advancement of cathode materials.[1,3,4] The epsilon polymorph of vanadyl phosphate ε-$VOPO_4$ is a promising candidate material as a high-capacity cathode, owing to its stability and demonstrated ability to reversibly incorporate more than one lithium per redox center, with a total theoretical capacity of 331 mAh/g for Li_2VOPO_4.[1,4−7] In fact, even with only the first lithium, the theoretical energy density is greater than that of $LiFePO_4$ due to its higher operating voltage near 4 V, making it more suitable for some portable electronics.[1] However, such a disparate two step voltage profile makes utilizing the full capacity in a practical device challenging.[4,8] A detailed understanding of the second lithium intercalation process may enable us to taylor the voltage and reduce this gap.

ε-$VOPO_4$ has a 3D tunnel structure consisting of 1D chains of corner sharing distorted VO_6 octahedra connected by PO_4 tetrahedra, also by corner sharing. The crystal structures of ε-$VOPO_4$ and the corresponding lithiated $LiVOPO_4$ and

Received: June 7, 2015
Revised: November 25, 2015

ACS Publications

DOI: 10.1021/acs.chemmater.5b02145

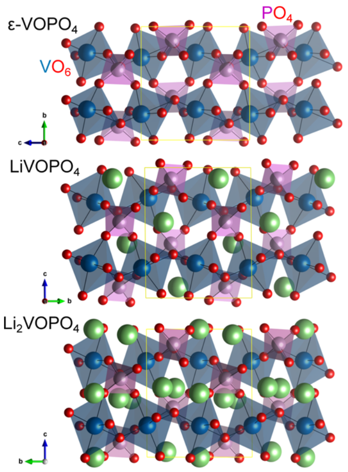

Figure 1. Crystal structures of ε-VOPO$_4$ and corresponding lithiated LiVOPO$_4$ and Li$_2$VOPO$_4$ phases.

Li$_2$VOPO$_4$ end phases are shown in Figure 1 (see also Table 1) rendered using the VESTA software.[9] The structural framework is essentially retained upon reaction with each lithium, differing only in the distortion of the metal phosphate framework.[10] ε-VOPO$_4$ has the most distorted VO$_6$ octahedra with the shortest vanadyl bond and the longest opposite V−O bond (1.572 and 2.556 Å, respectively) running along the chains. In LiVOPO$_4$, the vanadyl bond lengthens (1.626 Å), while the opposite V−O shortens significantly (2.240 Å) leading to more symmetrical VO$_6$ octahedra and considerably shorter V−V distance. Li ions in this compound occupy two distinct highly distorted five-coordinated sites.[11] The structure of Li$_2$VOPO$_4$ was only recently reported featuring the least distorted VO$_6$ octahedra (V−O bond lengths ranging from 1.98 to 2.04 Å). Li ions occupy five independent crystallographic sites in the channels of the structure, all different from that of LiVOPO$_4$.[10] Thus, Li ions of LiVOPO$_4$ have to move to different sites upon second Li intercalation. Also, the evidence of intermediate phases with 1.5 and 1.75 Li exists, but their structures are currently unknown.

As in the case of the olivine phosphates, the problem of the inherently low electronic conductivity of ε-VOPO$_4$ is overcome by the use of nanosized particles within the cathode. As the lithium is inserted at this scale, the electrochemical reaction can be largely affected by the interfacial chemistry at the nanoparticle surface. For example, particle size and shape are both known to influence the electrochemical performance of LiFePO$_4$.[1] However, given the importance of the cathode surface, there are remarkably few detailed experimental studies of the surface reactions.[13−17] While increased particle size of ε-VOPO$_4$ is generally found to lower the capacity, as in LiFePO$_4$, even some micron-size particles can achieve similar capacities at the same C/20 rate.[10,18] Therefore, it is clear that the low capacities are not exclusively due to particle size, suggesting that the surfaces play a more complicated role.[1]

Surfaces of ε-VOPO$_4$ remain unexplored experimentally. As a bulk material, the VOPO$_4$ system undergoes significant changes in crystal symmetry upon lithiation. Due to the reduced symmetry and wider range of possible chemical interactions at the surface, this region is expected to display even more complexity than the bulk. Recently, Li et al. predicted some particular LiVOPO$_4$ surfaces to have lower redox potentials than others, as well as differences from the bulk material.[19]

In this study, by performing X-ray photoelectron spectroscopy using both soft (XPS) and hard (HAXPES) X-rays, we are able to chemically distinguish and depth-resolve the interfacial phase transitions as a function of electrochemical lithiation. Core level analysis supports a straightforward two-phase reaction as the first lithium is intercalated. However, the intercalation of the first lithium is not yet completed when the second reaction begins, resulting in a pronounced lithium concentration gradient. Because of this limited ion diffusion, the ε-Li$_2$VOPO$_4$ phase is only formed near the surface of the equilibrated nanoparticles. This disruption of the kinetics is identified as a main contributor in limiting the realized capacity in our hydrothermally synthesized ε-VOPO$_4$. From inspection of the valence band region, we were able to monitor the evolution of ε-VOPO$_4$ after each full lithium insertion. Comparison with our hybrid density functional theory (DFT) calculations for ε-VOPO$_4$, ε-LiVOPO$_4$, and ε-Li$_2$VOPO$_4$ supports these assignments and reveals the nature of the lithium intercalation. Furthermore, the agreement between the measured valence band and density of states predicted by DFT demonstrates a methodology by which the computational methods can be assessed.

METHODOLOGY

Nanosized (average diameter ~100 nm) single crystals of ε-VOPO$_4$ were synthesized by the thermal decomposition of monoclinic H$_2$VOPO$_4$ and prepared as cathodes by combining the active material with carbon black (10 wt %) as a conductive additive and PVDF binder (10 wt %) in a mortar and pestle. NMP (1-methyl-2-pyrrolidinone, Aldrich) was added to create a paste, which was then laminated onto aluminum foil and vacuum-dried at 80 °C before use. The electrochemical properties were evaluated in a 2325-type coin cell with LiPF$_6$ electrolyte and lithium foil counter electrode. More detailed accounts of the synthesis and electrochemical properties of these cells are reported elsewhere.[6,20]

After reaching various points on the first discharge/charge cycle, each cell was carefully disassembled under inert conditions (either He or Ar glovebox) to extract the cathodes for analysis. While in the glovebox, the cathode surfaces were washed with DMC (dimethyl carbonate) to remove the residual electrolyte, dried, and sealed in plastic. When possible (most in-house measurements), samples were mounted on the experimental sample holder prior to sealing and removing from the glovebox. The samples were removed from the sealed plastic and promptly transferred into the respective experimental chambers to minimize the exposure to air and moisture.

The lab-based (soft) XPS was performed using a Phi VersaProbe 5000 system with a monochromated Al Kα source and hemispherical analyzer at the Analytical and Diagnostics Laboratory (ADL) at

Table 1. X-Ray Lattice Parameters of ε-VOPO$_4$, ε-LiVOPO$_4$, and ε-Li$_2$VOPO$_4$

phase	a (Å)	b (Å)	c (Å)	α (deg)	β (deg)	γ (deg)	V (Å^3)	space group
ε-VOPO$_4$[12]	7.266	6.893	7.265	90	115.34	90	328.87	Cc
ε-LiVOPO$_4$[11]	6.748	7.206	7.922	89.84	91.32	116.99	343.16	$P\bar{1}$
ε-Li$_2$VOPO$_4$[10]	7.199	7.101	7.777	89.82	89.81	116.32	356.36	$P\bar{1}$

Binghamton University. The core-levels (O 1s, V 2p, P 2p, Li 1s, C 1s) and the valence band (VB) region were measured with a pass energy of 23.5 eV, corresponding to an instrumental resolution of 0.5 eV from analyzing both the Au $4f_{7/2}$ and Fermi edge of the Au foil. A flood gun was used to achieve charge neutralization due to the insulating nature of the ε-$VOPO_4$.

The HAXPES measurements were performed at the bending magnet beamline X24A at the National Synchrotron Light Source (NSLS) using separate pieces of the same electrodes to ensure similar amounts of exposure. We noted no significant spatial variations across the electrodes in any photoemission experiments. An incident photon energy of ~4 keV and takeoff angle (TOA) of ~85° were employed to achieve the highest possible effective probing depth. The experimental chamber is equipped with a Scienta Electron Analyzer set to a pass energy of 200 eV operating in angular mode which results in a resolution comparable to the lab-based XPS. The binding energy scale for both the XPS and HAXPES were calibrated to the C 1s photoemission peak for carbon black with adventitious hydrocarbons at 284.6 eV.[21]

All calculations were performed using the periodic DFT code VASP,[22,23] in which a plane-wave basis set describes the valence electronic states. The Perdew−Burke−Ernzerhof[24] (PBE) gradient corrected functional was used to treat the exchange and correlation. The projector-augmented wave[25,26] (PAW) method was used to describe the interactions between the cores (Li:[He], V:[Ar], O:[He], and P:[He]) and the valence electrons. To counteract the self-interaction error and the band gap errors inherent to standard DFT functionals such as the PBE functional, higher levels of theory must be used. In this study, we have used the screened hybrid density functional developed by Heyd, Scuzeria, and Ernzerhof (HSE06),[27,28] as implemented in the VASP code.[29] HSE06 has been shown to yield improved decriptions of structure, band gap, and defect properties of a number of oxide semiconductors and battery materials.[30−46]

Adopting the nomenclature in which the lithiated phase is determined by the name of its delithiated form, structural optimizations of crystalline ε-$VOPO_4$,[12] ε-$LiVOPO_4$,[11] ε-Li_2VOPO_4,[10] Li_2O, and Li metal were performed using HSE06 at a series of volumes in order to calculate the equilibrium lattice parameters. In each case, the atomic positions, lattice vector, and cell angle were allowed to relax, while the total volume was held constant. The resulting energy volume curves were fitted to the Murnaghan equation of state to obtain the equilibrium bulk cell volume.[47] This approach minimizes the problems of Pulay stress and changes in basis set which can accompany volume changes in plane wave calculations. The Pulay stress affects the stress tensor which is not used in obtaining the optimized lattice vectors, and hence this approach is significantly more accurate than using the stress tensor to perform constant pressure optimization. Convergence with respect to k-point sampling and plane wave energy cutoff were checked, and a cutoff of 750 eV and a k-point density of 0.2 k/$Å^{-1}$ were found to be sufficient. Calculations were deemed to be converged when the forces on all the atoms were less than 0.01 eV $Å^{-1}$.

These calculations can also be used to predict the open circuit voltage during battery operation. As pointed out by Ceder and co-workers,[48] the average potential for intercalation between two compositions x_1 and x_2 can be obtained from the energy change in the reaction:

$$\mathrm{Li}_{x_1}\mathrm{VOPO}_4 + (x_2 - x_1)\mathrm{Li} \rightarrow \mathrm{Li}_{x_2}\mathrm{VOPO}_4$$

We calculated the average potential to be 4.03 and 2.39 V for the first and second lithiation steps, respectively. This is in reasonable agreement with our electrochemical analysis.

RESULTS AND DISCUSSION

Examining Disassembled Cells. To evaluate our methodology, we compared the core level XPS spectra collected from nanosized ε-$VOPO_4$ in pure powder form to our electrodes after cell disassembly. Figure 2 shows the XPS spectra from three samples: the ε-$VOPO_4$ powder, an electrode with minimal exposure, and an electrode with an additional 30 min of exposure to air. Each spectrum includes three main features; the O 1s peak and the spin orbit split V $2p_{3/2}$ and V $2p_{1/2}$ peaks. The V $2p_{3/2}$ is further split into two components representing the 5^+ (518.23 eV) and 4^+ (517.01 eV) oxidation states. Due to the extreme surface sensitivity of XPS coupled with the redox active nature of these samples, it was found that significant partial reduction of the vanadium cation to the 4^+ state occurs, which increases with duration of exposure. Along with this reduction, there is a concurrent increase in the O 1s feature at higher binding energy commonly attributed to adventitious surface oxygen. Both the V^{4+} and surface oxygen features are much less pronounced in the electrode with minimal exposure. This partial reduction is attributed to the additional chemistry involved in making the cathode slurry. The small V^{4+} contribution in the pure powder may be related to air exposure or it could represent a small amount of hydrogen remaining in the $VOPO_4$ framework from the sample growth resulting an a partial H_xVOPO_4 phase. We conclude that limiting cathode atmospheric exposure after cell disassembly to <5 min is sufficient to accurately attribute any vanadium reduction in our experiments to lithium intercalation after electrochemical cycling.

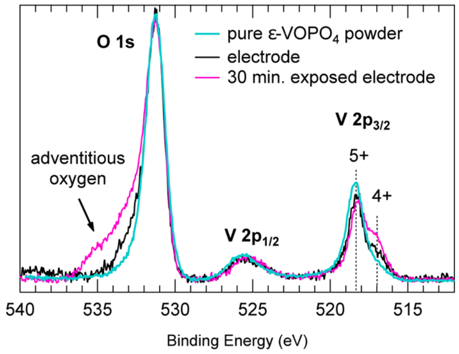

Figure 2. O 1s and V 2p XPS core levels obtained for pure ε-$VOPO_4$ powder, a synthesized ε-$VOPO_4$ electrode with minimal exposure, and a ε-$VOPO_4$ electrode after an additional 30 min air exposure.

First Discharge/Charge Cycle. Figure 3a shows the galvanostatic discharge−charge curve from 3.8 to 1.5 V for the first cycle of the ε-$VOPO_4$ cells at 0.082 mA/cm^2. The discharge voltage profile exhibits two plateaus, corresponding to the V^{5+}/V^{4+} (~3.8 V) and V^{4+}/V^{3+} (starting at ~2.5 V) redox couples. The calculated voltages for each step (dotted lines) show good agreement with the first cycle. The capacities for each lithium insertion here are similar to previous works, though notably, these are significantly lower than the theoretical lithium capacities, which are 165 and 331 mAh/g for the first and second lithium inclusion, respectively. The cells were stopped at different points along the first full cycle, labeled A−E (discharge) and F−I (charge). The surface of the control electrode A was exposed to the electrolyte and washed as the others were, even though it was not subjected to any electrochemical cycling, for best comparison.

The corresponding XPS spectra collected from each of these samples for the O 1s and V 2p core region are shown in Figure 3b. First, we note the stark changes in the V $2p_{3/2}$ over the first cycle. There is a general shift toward lower binding energy during discharge and back to higher binding energy during charging, consistent with reduction and subsequent oxidation of the vanadium cation. This correlates well with an increasing and

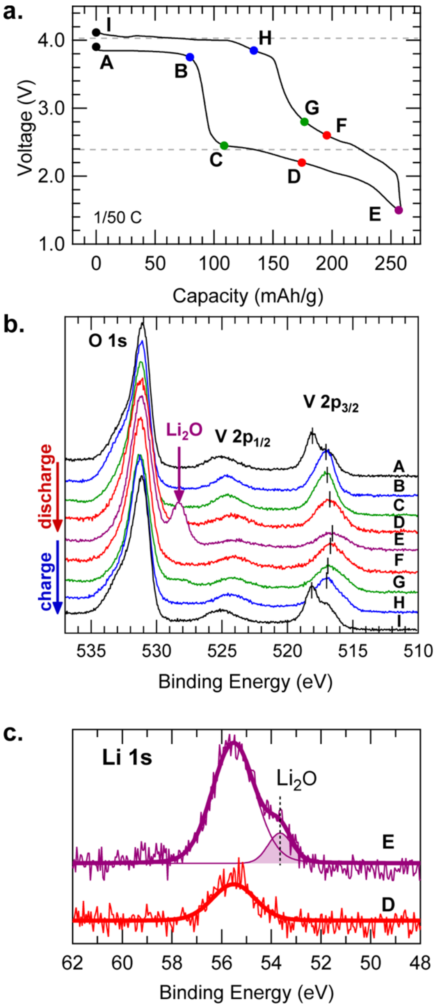

Figure 3. (a) First galvanostatic curve to 1.5 V typical of ε-$VOPO_4$ cells with labels A−I indicating stopping points where each cell was disassembled. (b) O 1s and V 2p XPS core levels obtained for ε-$VOPO_4$ electrodes after increasing amounts of discharge/charge. (c) Li 1s XPS core level obtained for electrodes D and E showing the main Li_xVOPO_4 peak (55.52 eV) and the appearance of the Li_2O peak (53.65 eV).

then decreasing intensity observed in the Li 1s core level. We note that the P 2p core level line shape (shown in Supporting Information) remained constant as a function of discharge and charge. This suggests that the PO_4^{3-} groups are robust, confirming the stability of the PO_4 polyhedra. This is discussed further below.

Another distinct feature is the presence of a new peak centered at 528.28 eV below the main O 1s peak after discharge to 1.5 V (electrode E), indicated in Figure 3b. This peak is assigned to the O 1s core level in Li_2O, signifying the formation of a foreign species at the cathode. This assignment is supported by the concurrent emergence of a distinct Li 1s feature at 53.65 eV, almost 2 eV below the main peak representing lithium in Li_xVOPO_4 at 55.52 eV, shown in Figure 3c. Both of these features are in agreement with reported values for Li_2O.[49,50] Along with these changes in electrode E, there is a relative decrease in the intensity of the P 2p and V 2p features, as well as a slight decrease in the C 1s signal from the carbon black. This is ascribed to the formation of the Li_2O at the cathode surface, i.e. the interface with the electrolyte, causing an attenuation of the electrons originating from the composite cathode beneath. From these relative changes in intensity and the overall surface sensitivity of photoemission, we estimate the Li_2O layer to be <1 nm in thickness; however we do not expect this to be a uniform continuous film. Additional XPS measurements have ruled out air exposure as a possible origin of the Li_2O formation (refer to Supporting Information).

There have been reports of surface Li_2O formation as a solid-electrolyte interphase (SEI) constituent on electrode materials formed upon lithiation.[16,51,52] These reports all attribute this to a breakdown of the electrolyte. It is possible that this is the case here when considering the low operating voltage of the second lithium insertion. However, it is also possible that the Li_2O is a product of decomposition of the cathode material due to overdischarge, since the extended electrochemistry is not well-studied discharging past 2 V.[20] The similar $LiFePO_4$ is known to decompose to Li_3PO_4 and metallic Fe below 1 V, but the decomposition products of ε-$VOPO_4$ are not well-known.[53,54] Interestingly, the features associated with Li_2O are not present after charging. This is suggestive that the Li_2O layer is unstable on the Li_xVOPO_4 cathode surface; however the mechanism of this formation and decomposition is not studied here and warrants future investigation. Despite this interfacial species formation, the fully cycled electrode I displays nearly identical spectra as the nondischarged electrode A (shown in detail in the Supporting Information). This demonstrates the recovery capability of ε-$VOPO_4$ to the fully delithiated state, at least for the first cycle. This finding rules against the decomposition of the cathode material as the origin of the Li_2O.

Depth-Resolved Analysis. To further examine the interfacial chemistry as each lithium ion is inserted (approaching the Li_2VOPO_4 end point), we complement our XPS measurements with HAXPES to take advantage of the deeper probing depth. Estimated from the universal inelastic mean free path curve, 95% of V $2p_{3/2}$ core level photoelectrons in XPS (KE ≈ 970 eV) derive from less than ∼3 nm. However, in HAXPES, since the photoelectrons have greater kinetic energy (KE ≈ 3.5 keV), we are able to access information from up to ∼12 nm below the surface.

Figure 4a shows the V $2p_{3/2}$ core level obtained from XPS (left) and HAXPES (right) for electrodes A−E along the first discharge curve scaled such that the total area under each curve is equal to one. As in XPS, the HAXPES spectra of the noncycled electrode A and fully cycled electrode I display nearly identical oxidation state profiles, further indicating high reversibility when discharged to 1.5 V (shown in Supporting Information). Electrode A does show a slightly lower V^{4+} weight in the HAXPES compared to the XPS spectra. However, this can be expected because the nanoparticle subsurface is likely less sensitive to the initial reduction from cathode synthesis. Following discharge, electrodes B and C show almost identical lineshapes between the XPS and HAXPES spectra indicating uniform lithium intercalation up until that point of the discharging process. After discharge to points D and E there is a pronounced lag of the vanadium cation reduction in the HAXPES signifying that the second lithium does not intercalate uniformly throughout the nanoparticle. Considering that photoemission is spatially averaging over many nanoparticles and the nanoparticles are in no particular orientation, we interpret this as a radial gradient of lithium with greater lithium concentration nearer the outer surface.

Peak fitting of the V $2p_{3/2}$ region in both XPS and HAXPES was carried out for quantitative analysis of the vanadium reduction along the galvanostatic discharge curve. All fits were

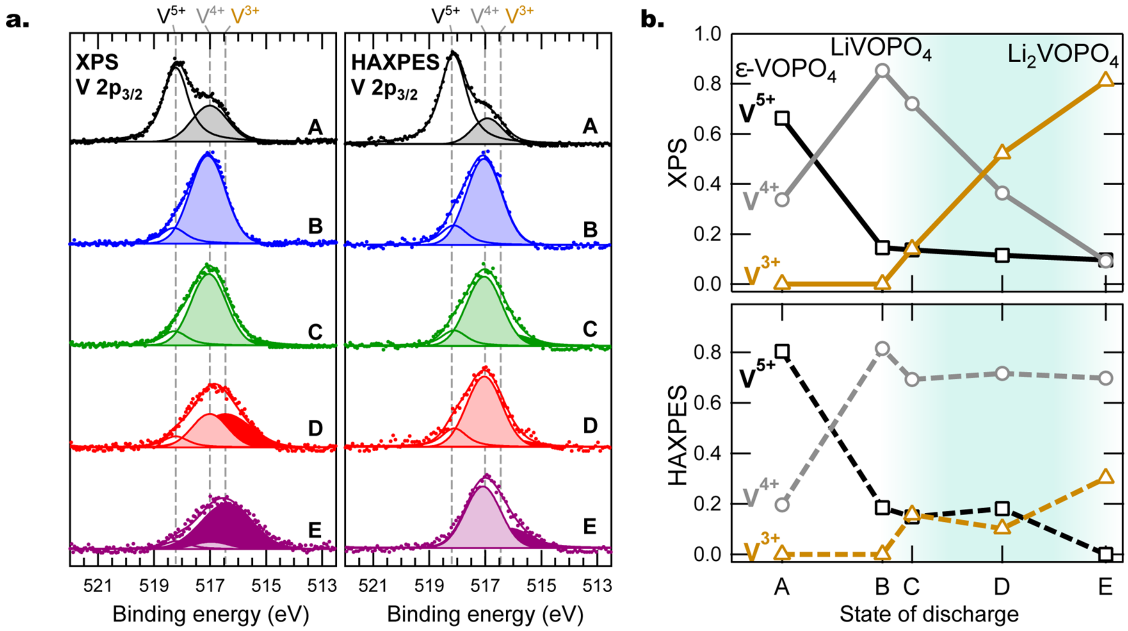

Figure 4. (a) Peak fitting of the V $2p_{3/2}$ core level obtained from XPS (left) and HAXPES (right) for electrodes A−E along the first discharge curve scaled such that the total area under each curve is equal to 1. (b) Vanadium oxidation state ratios obtained from peak fitting XPS (top) and HAXPES (bottom) spectra for increasing depth of discharge.

performed including the O 1s and V 2p peaks concurrently after the removal of a Shirley-like background. Voigt lineshapes were used with Gaussian and Lorentzian contributions constrained to be the same for each unique peak across both (XPS/HAXPES) data sets. The fits revealed three discrete V $2p_{3/2}$ peaks at 518.23, 517.01, and 516.45 eV assigned to vanadium 5^+, 4^+, and 3^+ oxidation states, respectively. The most reliable method of assigning oxidation states in XPS of vanadium oxides is the energetic separation from the main O 1s peak (531.1 eV). The separations and lineshapes observed in our spectra are in exceptionally good agreement with the vanadium oxide studies of Silversmit et al.,[55] although we note such precise agreement is likely fortuitous since we are comparing an oxide group to this oxyphosphate group. Nevertheless, the discrete energetic separations from the V^{5+} to the reduced counterparts should not deviate greatly from other systems.

The relative areas of each V $2p_{3/2}$ peak are plotted in Figure 4b for each electrode along the discharge curve. Aside from the exposure induced surface reduction, it is clear that there is no evidence of inhomogeneity of the lithium intercalation over the first redox plateau at least within the first ∼12 nm. This is consistent with a straightforward two-phase reaction from ε-$VOPO_4$ to $LiVOPO_4$ as previously suggested,[10] with the vanadium almost entirely reduced to a 4^+ oxidation state in both the surface and subsurface regions.

As the intercalation process proceeds toward the incorporation of the second lithium, i.e. from electrode C to E, there is a marked difference. The XPS shows a smooth crossover of the vanadium oxidation state from 4^+ to 3^+, while the HAXPES shows only relatively small changes across these electrodes. At the deepest discharge, while the vanadium oxidation state is almost exclusively 3^+ within the first few nanometers of the surface, consistent with formation of Li_2VOPO_4, the subsurface probing of HAXPES indicates only about 30% formal valence of V^{3+}. We estimate that there is only Li_2VOPO_4 present within the first 3−5 nm of the nanoparticles, since the majority of the HAXPES signal comes from nearer the surface, due to the exponentially decaying profile of the escaping photoelectrons. This is evidence of limited ion diffusion, i.e., a subsurface of Li_xVOPO_4 where $1 < x < 2$, with less lithium toward the center of the nanoparticle.

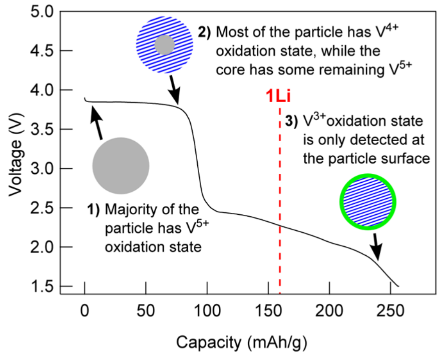

Figure 5. A qualitative schematic showing the vanadium oxidation states of an average ε-$VOPO_4$ nanoparticle at key points along the first discharge curve. The theoretical capacity of 165 mAh/g for one full lithium intercalation ($LiVOPO_4$) is indicated.

The composition and spatial distribution of an average nanoparticle can be determined from our depth-resolved analysis. Figure 5 shows a cross-sectional schematic of a single ε-$VOPO_4$ nanoparticle at three points along the first discharge. At the beginning of the high voltage plateau (point 1), the majority of the particle has a vanadium oxidation of 5^+. At the end of the high voltage plateau (point 2), both the surface and subsurface show predominantly V^{4+}. However, the realized capacity is far short of the theoretical capacity for one full lithium insertion of 165 mAh/g, revealing that the core of the particle must remain in the V^{5+} oxidation state. This core−shell like structure between these two phases indicates a disruption of disrupted kinetics occurring during the first lithium insertion. Furthermore, the drop to the low voltage plateau indicates the

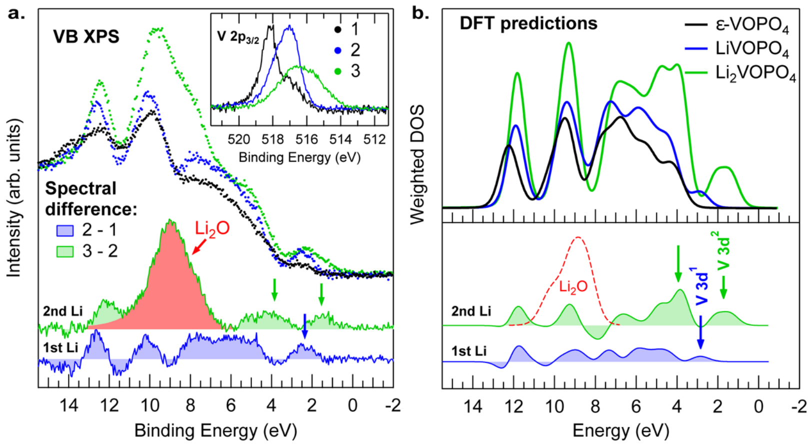

Figure 6. (a) Valence band XPS of three ε-$VOPO_4$ electrodes most representative of the three end phases labeled 1, 2, and 3 with respective vanadium oxidation states predominantly 5^+, 4^+, and 3^+. Plotted on the bottom are the difference spectra from 1 to 2 and 2 to 3. (b) The weighted and broadened density of states from DFT calculations of ε-$VOPO_4$ and its lithiated $LiVOPO_4$ and Li_2VOPO_4 phases. Plotted on the bottom are the difference spectra representing the addition of each full lithium.

onset of the second reaction. At this point, V^{3+} begins to form on the particle surface, before the V^{5+} core is reduced. Finally, at the end of the low voltage plateau (point 3), the V^{3+} is restricted to the outermost surface of the particle, despite the incorporation of a significant amount of more lithium.

Evolution of Electronic Structure. While the core levels contain information regarding transition metal oxidation state, the specific material phase can be verified by comparison between the measured valence band and density functional theory predicted density of states. From our core-level analysis, the V 2p peak displays varying amounts of three distinct vanadium oxidation states, i.e., 5^+, 4^+, and 3^+. To this point, these have been interpreted as the incorporation of lithium to form the ε-$VOPO_4$, $LiVOPO_4$, and Li_2VOPO_4 phases; however it is important to rule out other possible vanadium containing species, especially after electrochemical cycling.

Furthermore, in the effort to understand cathode materials as they are (de)lithiated, the study of the structural evolution has routinely been of central focus, and these efforts have been remarkably successful. However, due to the strong electron correlation effects of the partially filled d states in the transition metals, a complete understanding cannot be obtained by the crystal structure alone. For example, the operating voltage, ion/electron transport properties, and phase stability are each dictated by both the structural properties and the electronic states in the vicinity of the Fermi level.[1,3] Therefore, direct comparison of the measured valence band with DFT predictions allows for not only the identification of chemical species but also accurate orbital assignment of distinct valence band features that can be monitored as a function of delithiation.

At the surface of the nanoparticles, each of the three vanadium oxidation states can be accessed using soft XPS. Here, an additional set of three electrodes have intentionally been discharged to each represent a distinct oxidation state. Figure 6a shows the valence band XPS spectra of these three electrodes (labeled 1−3), with the V 2p core level XPS shown in the inset. Additional core level XPS is shown in the Supporting Information (O 1s, V 2p, and Li 1s).

Due to the relatively little valence band structure seen for carbon black and low concentration of the binder, there is no significant spectral contamination. The prevalent valence band structure of these electrodes is very similar to that of the olivine $LiMnPO_4$ and $LiFePO_4$ systems and consists of two P 3s and 3p derived peaks at ∼12 and 10 eV, along with a largely O 2p derived band centered at 6 eV below the Fermi level.[45,56,57] Between the O 2p band and the Fermi level, the V 3d states increase with lithium insertion and are largest for electrode 3. In addition, there is increased spectral weight at ∼9 eV in electrode 3 compared to electrodes 1 and 2. Previous studies of $MnPO_4$ and Mn_2PO_7 have shown significant orbital rearrangement in the valence band region associated with the difference between PO_4^{3-} and $P_2O_7^{4-}$ groups.[45] Here, we do not observe evidence of any pyrophosphate contributions near 15 eV. This finding is consistent with the lack of any changes in the P 2p core level spectra. Instead, we consider this contribution at ∼9 eV as a result of Li_2O formation on the surface (Figure 3c).

To confirm our chemical assignments based on vanadium oxidation state, we compared our valence band spectra with the calculated electronic structure from DFT. Figure 6b shows the DFT predicted valence band spectra for ε-$VOPO_4$ and its corresponding $LiVOPO_4$ and Li_2VOPO_4 lithiated phases. These predictions are obtained by summing the orbital projected density of states after weighting by the corresponding photoionization cross-section[58] and then convolving the sum with a Voigt profile (0.1 eV Lorentzian width, 0.5 eV Gaussian width) to match the experimental resolution. Also included are the predicted spectra for Li_2O to account for a small amount of surface Li_2O observed in the core level XPS only in the deepest discharged electrode 3. Our predicted Li_2O line shape is in good agreement with experimental observations, and thus the large increase of spectral weight near 9 eV is not representative of any orbital rearrangements inherent to the Li_2VOPO_4 phase.[59,60] We note that in our DFT, the Fermi level is at the valence band maximum. In Figure 6b, the predicted spectra were rigidly shifted to match the experimentally determined Fermi level.

The valence band spectra of the ε-$VOPO_4$ end phases are in exceptional agreement with the electronic structure predictions, after the Li_2O is considered. This agreement provides more conclusive evidence of reaching the $LiVOPO_4$ and Li_2VOPO_4 end phases than the vanadium oxidation states alone. Common to all three phases in the DFT are a broad O 2p anion band spanning about 4−9 eV, and two sharper features near 10 and

12.5 eV. The latter two are confirmed as P 3p and 3s hybridized with the O 2p states, respectively. The main difference between these phases is highlighted by the additional feature above the valence band maximum of ε-$VOPO_4$ associated with the V 3d states becoming more occupied with the insertion of each lithium. The nondischarged ε-$VOPO_4$ spectra do however deviate slightly from the predicted spectra in this region. There is some observed weight in the V 3d region that is not predicted by the DFT. This is explained by partial filling of the first unoccupied V $3d^1$ state due to the tendency of the pristine material to reduce slightly from surface exposure inherent to the electrode processing, and it indeed correlates with the small amount of V^{4+} observed in the V $2p_{3/2}$ core level.

The difference spectra are included to highlight the evolution of the electronic structure after the first and second full lithium is intercalated, thus representing the

$$V^{5+}OPO_4 + Li^+ + e^- \rightarrow LiV^{4+}OPO_4$$

and

$$LiV^{4+}OPO_4 + Li^+ + e^- \rightarrow Li_2V^{3+}OPO_4$$

reactions, respectively. The addition of the first lithium is shown to cause significant changes to the valence band structure. There is an increase and slight redistribution of spectral weight in all the oxygen and phosphorus bonding states. This is attributed to the large change in crystal structure upon the transition from ε-$VOPO_4$ (Monoclinic *Cc*) to $LiVOPO_4$ (Triclinic $P\bar{1}$) along with an increase of octahedral symmetry leading to a ~ 7% contraction along the VO_6 chains all contributing to increased local bonding. This shows that the V−O bonds, especially along the VO_6 chains contribute to the stability of this structure. Along with these changes is a clear increase of the discrete V $3d^1$ states about 1.5 eV above the top of O 2p band due to the electron transfer from the lithium to the vanadium cation.

After the second lithium is incorporated there is continued filling of the vanadium d states where a V 3 d^2 peak is observed above that of the V 3 d^1 states in both the DFT and XPS. After considering the contribution of the Li_2O (highlighted in red) to the difference spectra, there are only small changes in the deeper oxygen and phosphorus bonding states. This is likely because the VO_6 chains only contract an additional ~1.5% upon transitioning from $LiVOPO_4$ to Li_2VOPO_4 while the space group is preserved. Additional weight, however, is observed at the top of the O 2p band (~4 eV) as the V 3 d^2 states are filled, indicating that the electron transfer is largely shared by between the oxygen and vanadium. This covalent character should contribute to increased stability of this material upon lithiation.

Both the redox active vanadium 3 d^1 and 3 d^2 states are confirmed to lie well above the broad O 2p anion band rather than pinned in the O 2p band or below it. This is the preferred case for thermodynamic stability.[3,61] Both of these redox active states are also sufficiently far below the Li^+/Li^0 potential such that they can both be accessed.

CONCLUSIONS

Our findings support a two-phase reaction from ε-$VOPO_4$ to $LiVOPO_4$ following a core−shell like structure. In our hydrothermally synthesized ε-$VOPO_4$, we find that the second lithium reaction begins before the full incorporation of the first lithium. This results in a pronounced lithium gradient within the nanoparticles, with the ε-Li_2VOPO_4 phase only forming near the surface. These assignments are supported by both the core level and valence band XPS as well as our hybrid DFT calculations. This restricted diffusion at the nanoparticle surface is sufficient to effect the macroscopic properties of the cathode material and thus could contribute to the relatively low capacities reported. This should be considered in order to achieve capacities closer to the theoretical limit.

Our observation of a Li gradient formation is quite different from the studies of Bianchini et al. where ε-$LiVOPO_4$ is used as the starting material and is shown to electrochemically reach the Li_2VOPO_4 phase in the bulk.[10] Our findings indicate that using ε-$VOPO_4$ as a starting material may be intrinsically different (e.g., due to defects in the $LiVOPO_4$ phase) when electrochemically lithiating to Li_2VOPO_4. Such defects could be responsible for the disruption of the Li^+ kinetics or electronic transport and cause the Li gradient to occur.

Despite both the Li gradient and the surface formation of Li_2O, these cathodes exhibit full recovery to the delithiated ε-$VOPO_4$ state for the first full cycle. Furthermore, comparison with our hybrid-DFT calculations shows good agreement and confirms the orbital character of distinct valence band features. The evolution of the electronic structure provides insight into fundamental properties affecting the electrochemical performance of these cathodes.

ASSOCIATED CONTENT

Ⓢ Supporting Information

The Supporting Information is available free of charge on the ACS Publications website at DOI: 10.1021/acs.chemmater.5b02145.

> P 2p core level XPS; evidence ruling out air exposure as the cause of Li_2O formation; additional V 2p core level XPS and HAXPES; correlation of vanadium reduction and Li 1s XPS peak intensity; core level XPS of electrodes presented in Figure 5 (PDF)

AUTHOR INFORMATION

Corresponding Author

*E-mail: lpiper@binghamton.edu.

Notes

The authors declare no competing financial interest.

ACKNOWLEDGMENTS

This work was supported as part of NECCES, an Energy Frontier Research Center funded by the U.S. Department of Energy, Office of Science, Office of Basic Energy Sciences under Award Number DE-SC0012583. The NSLS is supported by the U.S. Department of Energy, Office of Science, Office of Basic Energy Sciences, under Contract No. DE-AC02-98CH10886. The simulations made use the ARCHER supercomputer through membership of the UK's HPC Materials Chemistry Consortium (EPSRC grant EP/L000202).

REFERENCES

(1) Whittingham, M. S. Ultimate Limits to Intercalation Reactions for Lithium Batteries. *Chem. Rev.* **2014**, *114*, 11414−11443. PMID: 25354149.

(2) Chen, J. Recent Progress in Advanced Materials for Lithium Ion Batteries. *Materials* **2013**, *6*, 156−183.

(3) Goodenough, J. B.; Kim, Y. Challenges for Rechargeable Li Batteries. *Chem. Mater.* **2010**, *22*, 587−603.

(4) Melot, B. C.; Tarascon, J.-M. Design and Preparation of Materials for Advanced Electrochemical Storage. *Acc. Chem. Res.* **2013**, *46*, 1226−1238. PMID: 23282038.

(5) Whittingham, M. S.; Song, Y.; Lutta, S.; Zavalij, P. Y.; Chernova, N. A. Some transition metal (oxy)phosphates and vanadium oxides for lithium batteries. *J. Mater. Chem.* **2005**, *15*, 3362−3379.

(6) Song, Y.; Zavalij, P. Y.; Whittingham, M. S. ε-VOPO$_4$: Electrochemical Synthesis and Enhanced Cathode Behavior. *J. Electrochem. Soc.* **2005**, *152*, A721−A728.

(7) Mueller, T.; Hautier, G.; Jain, A.; Ceder, G. Evaluation of Tavorite-Structured Cathode Materials for Lithium-Ion Batteries Using High-Throughput Computing. *Chem. Mater.* **2011**, *23*, 3854−3862.

(8) Ateba Mba, J.-M.; Masquelier, C.; Suard, E.; Croguennec, L. Synthesis and Crystallographic Study of Homeotypic LiVPO4F and LiVPO4O. *Chem. Mater.* **2012**, *24*, 1223−1234.

(9) Momma, K.; Izumi, F. VESTA: a three-dimensional visualization system for electronic and structural analysis. *J. Appl. Crystallogr.* **2008**, *41*, 653.

(10) Bianchini, M.; Ateba-Mba, J. M.; Dagault, P.; Bogdan, E.; Carlier, D.; Suard, E.; Masquelier, C.; Croguennec, L. Multiple phases in the [varepsilon]-VPO4O-LiVPO4O-Li2VPO4O system: a combined solid state electrochemistry and diffraction structural study. *J. Mater. Chem. A* **2014**, *2*, 10182−10192.

(11) Lavrov, A. V.; Nikolaev, V. P.; Sadikov, G. G.; Poraikoshits, M. A. Synthesis and Crystal Structure of Mixed Vanadyl and Lithium Ortho-Phosphate, LiVOPO4. *Doklady Akademii Nauk Sssr* **1982**, *266*, 343−346.

(12) Girgsdies, F.; Dong, W.-S.; Bartley, J.; Hutchings, G.; Schlogl, R.; Ressler, T. The crystal structure of ε-VOPO4. *Solid State Sci.* **2006**, *8*, 807−812. Special issue in honor of H.G von Schnering.

(13) Rho, Y.-H.; Nazar, L. F.; Perry, L.; Ryan, D. Surface Chemistry of LiFePO4 Studied by Mïssbauer and X-Ray Photoelectron Spectroscopy and Its Effect on Electrochemical Properties. *J. Electrochem. Soc.* **2007**, *154*, A283−A289.

(14) Dedryvère, R.; Maccario, M.; Croguennec, L.; Le Cras, F.; Delmas, C.; Gonbeau, D. X-Ray Photoelectron Spectroscopy Investigations of Carbon-Coated LixFePO4Materials. *Chem. Mater.* **2008**, *20*, 7164−7170.

(15) Park, K.-S.; Xiao, P.; Kim, S.-Y.; Dylla, A.; Choi, Y.-M.; Henkelman, G.; Stevenson, K. J.; Goodenough, J. B. Enhanced Charge-Transfer Kinetics by Anion Surface Modification of LiFePO4. *Chem. Mater.* **2012**, *24*, 3212−3218.

(16) Malmgren, S.; Ciosek, K.; Hahlin, M.; Gustafsson, T.; Gorgoi, M.; Rensmo, H.; Edström, K. Comparing anode and cathode electrode/electrolyte interface composition and morphology using soft and hard X-ray photoelectron spectroscopy. *Electrochim. Acta* **2013**, *97*, 23−32.

(17) Chung, S.-Y.; Choi, S.-Y.; Kim, T.-H.; Lee, S. Surface-Orientation-Dependent Distribution of Subsurface Cation-Exchange Defects in Olivine-Phosphate Nanocrystals. *ACS Nano* **2015**, *9*, 850−859. PMID: 25565086.

(18) Harrison, K. L.; Manthiram, A. Microwave-Assisted Solvothermal Synthesis and Characterization of Various Polymorphs of LiVOPO4. *Chem. Mater.* **2013**, *25*, 1751−1760.

(19) Li, Y.; Zhang, J.; Yang, F.; Liang, J.; Sun, H.; Tang, S.; Wang, R. Morphology and surface properties of LiVOPO4: a first principles study. *Phys. Chem. Chem. Phys.* **2014**, *16*, 24604−24609.

(20) Chen, Z.; Chen, Q.; Chen, L.; Zhang, R.; Zhou, H.; Chernova, N. A.; Whittingham, M. S. Electrochemical Behavior of Nanostructured ε-VOPO$_4$ over Two Redox Plateaus. *J. Electrochem. Soc.* **2013**, *160*, A1777−A1780.

(21) Lu, Y.-C.; Mansour, A. N.; Yabuuchi, N.; Shao-Horn, Y. Probing the Origin of Enhanced Stability of âĂlPO4âĂİ Nanoparticle Coated LiCoO2 during Cycling to High Voltages: Combined XRD and XPS Studies. *Chem. Mater.* **2009**, *21*, 4408−4424.

(22) Kresse, G.; Furthmüller, J. Efficient iterative schemes for ab initio total-energy calculations using a plane-wave basis set. *Phys. Rev. B: Condens. Matter Mater. Phys.* **1996**, *54*, 11169−11186.

(23) Kresse, G.; Hafner, J. *Ab initio* molecular-dynamics simulation of the liquid-metal-amorphous-semiconductor transition in germanium. *Phys. Rev. B: Condens. Matter Mater. Phys.* **1994**, *49*, 14251−14271.

(24) Perdew, K. E. M.; Burke, J. P. Generalized gradient approximation made simple. *Phys. Rev. Lett.* **1996**, *77*, 3865−3868.

(25) Blöchl, P. E. Projector augmented-wave method. *Phys. Rev. B: Condens. Matter Mater. Phys.* **1994**, *50*, 17953.

(26) Kresse, G.; Joubert, D. From ultrasoft pseudopotentials to the projector augmented-wave method. *Phys. Rev. B: Condens. Matter Mater. Phys.* **1999**, *59*, 1758−1775.

(27) Heyd, S.; Scuseria, G. E.; Ernzerhof, M. Hybrid functionals based on a screened Coulomb potential. *J. Chem. Phys.* **2003**, *118*, 8207−8215.

(28) Krukau, A. V.; Vydrov, O. A.; Izmaylov, A. F.; Scuseria, G. E. Influence of the exchange screening parameter on the performance of screened hybrid functionals. *J. Chem. Phys.* **2006**, *125*, 224106.

(29) Paier, J.; Marsman, M.; Hummer, K.; Kresse, G.; Gerber, I. C.; Ángyán, J. G. Screened Hybrid Density Functionals Applied to Solids. *J. Chem. Phys.* **2006**, *124*, 154709−154713.

(30) Heyd, J.; Scuseria, G. E. Efficient hybrid density functional calculations in solids: Assessment of the Heyd-Scuseria-Ernzerhof screened Coulomb hybrid functional. *J. Chem. Phys.* **2004**, *121*, 1187−1192.

(31) Heyd, J.; Peralta, J. E.; Scuseria, G. E.; Martin, R. L. Energy band gaps and lattice parameters evaluated with the Heyd-Scuseria-Ernzerhof screened hybrd functional. *J. Chem. Phys.* **2005**, *123*, 174101.

(32) Da Silva, J. L. F.; Ganduglia-Pirovano, M. V.; Sauer, J.; Bayer, V.; Kresse, G. Hybrid functionals applied to rare earth oxides: The example of ceria. *Phys. Rev. B: Condens. Matter Mater. Phys.* **2007**, *75*, 045121.

(33) Walsh, A.; Da Silva, J. L. F.; Yan, Y.; Al-Jassim, M. M.; Wei, S. H. Origin of electronic and optical trends in ternary $In_2O_3(ZnO)_n$ transparent conducting oxides (n = 1,3,5): Hybrid density functional theory calculations. *Phys. Rev. B: Condens. Matter Mater. Phys.* **2009**, *79*, 073105.

(34) Chen, S.; Gong, Z. G.; Walsh, A.; Wei, S. H. Crystal and electronic band structure of Cu_2ZnSnX_4 (X = S and Se) photovoltaic absorbers: First-principles insights. *Appl. Phys. Lett.* **2009**, *94*, 041903.

(35) Allen, J. P.; Scanlon, D. O.; Watson, G. W. Electronic Structure of Mixed-Valence Silver Oxide AgO from Hybrid Density-Functional Theory. *Phys. Rev. B: Condens. Matter Mater. Phys.* **2010**, *81*, 161103(R).

(36) Scanlon, D. O.; Watson, G. W. Conductivity Limits in $CuAlO_2$ from Screened-Hybrid Density Functional Theory. *J. Phys. Chem. Lett.* **2010**, *1*, 3195−3199.

(37) Janesko, B. G.; Henderson, T. M.; Scuseria, G. E. Screened Hybrid Density Functionals for Solid-State Chemistry and Physics. *Phys. Chem. Chem. Phys.* **2009**, *11*, 443−454.

(38) Scanlon, D. O.; Watson, G. W. Undoped n-Type Cu2O: Fact or Fiction? *J. Phys. Chem. Lett.* **2010**, *1*, 2582−2585.

(39) Peralta, J. E.; Heyd, J.; Scuseria, G. E.; Martin, R. L. Spin-Orbit Splittings and Energy Band Gaps Calculated with the Heyd-Scuseria-Ernzerhof Screened Hybrid Functional. *Phys. Rev. B: Condens. Matter Mater. Phys.* **2006**, *74*, 073101.

(40) Scanlon, D. O.; Morgan, B. J.; Watson, G. W.; Walsh, A. Acceptor Levels in p-type Cu_2O: Rationalizing Theory and Experiment. *Phys. Rev. Lett.* **2009**, *103*, 096405.

(41) Stroppa, A.; Kresse, G. Unraveling the Jahn-Teller effect in Mn-doped GaN using the Heyd-Scuseria-Ernzerhof hybrid functional. *Phys. Rev. B: Condens. Matter Mater. Phys.* **2009**, *79*, 201201.

(42) Stroppa, A.; Picozzi, S. Hybrid functional study of improper multiferroics. *Phys. Chem. Chem. Phys.* **2010**, *12*, 5405−5416.

(43) Scanlon, D. O.; Watson, G. W. Uncovering the complex behaviour of hydrogen in Cu_2O. *Phys. Rev. Lett.* **2011**, *106*, 186403.

(44) Ong, S. P.; Chevrier, V. L.; Ceder, G. Comparison of small polaron migration and phase separation in olivine $LiMnPO_4$ and $LiFePO_4$ using hybrid density functional theory. *Phys. Rev. B: Condens. Matter Mater. Phys.* **2011**, *83*, 075112.

(45) Huang, Y.; Fang, J.; Omenya, F.; O'Shea, M.; Chernova, N. A.; Zhang, R.; Wang, Q.; Quackenbush, N. F.; Piper, L. F. J.; Scanlon, D. O.; Whittingham, M. S. Understanding the stability of MnPO4. *J. Mater. Chem. A* **2014**, *2*, 12827−12834.

(46) Hoang, K.; Johannes, M. D. Defect chemistry in layered transition-metal oxides from screened hybrid density functional calculations. *J. Mater. Chem. A* **2014**, *2*, 5224−5235.

(47) Murnaghan, F. D. The Compressibility of Media under Extreme Pressures. *Proc. Natl. Acad. Sci. U. S. A.* **1944**, *30*, 244−247.

(48) Ceder, G.; Chiang, Y. M.; Sadoway, D. R.; Aydinol, M. K.; Jang, Y. I.; Huang, B. Identification of cathode materials for lithium batteries guided by first-principles calculations. *Nature* **1998**, *392*, 694−696.

(49) Harilal, S.; Allain, J.; Hassanein, A.; Hendricks, M.; Nieto-Perez, M. Reactivity of lithium exposed graphite surface. *Appl. Surf. Sci.* **2009**, *255*, 8539−8543.

(50) Yao, K. P. C.; Kwabi, D. G.; Quinlan, R. A.; Mansour, A. N.; Grimaud, A.; Lee, Y.-L.; Lu, Y.-C.; Shao-Horn, Y. Thermal Stability of Li2O2 and Li2O for Li-Air Batteries: In Situ XRD and XPS Studies. *J. Electrochem. Soc.* **2013**, *160*, A824−A831.

(51) Philippe, B.; Dedryvère, R.; Allouche, J.; Lindgren, F.; Gorgoi, M.; Rensmo, H.; Gonbeau, D.; Edström, K. Nanosilicon Electrodes for Lithium-Ion Batteries: Interfacial Mechanisms Studied by Hard and Soft X-ray Photoelectron Spectroscopy. *Chem. Mater.* **2012**, *24*, 1107−1115.

(52) Song, M.-S.; Kim, R.-H.; Baek, S.-W.; Lee, K.-S.; Park, K.; Benayad, A. Is Li4Ti5O12 a solid-electrolyte-interphase-free electrode material in Li-ion batteries? Reactivity between the Li4Ti5O12 electrode and electrolyte. *J. Mater. Chem. A* **2014**, *2*, 631−636.

(53) Yang, S.; Song, Y.; Ngala, K.; Zavalij, P. Y.; Whittingham, M. S. Performance of LiFePO4 as lithium battery cathode and comparison with manganese and vanadium oxides. *J. Power Sources* **2003**, *119−121*, 239−246. Selected papers presented at the 11th International Meeting on Lithium Batteries.

(54) Shu, J.; Shui, M.; Xu, D.; Wang, D.; Ren, Y.; Gao, S. A comparative study of overdischarge behaviors of cathode materials for lithium-ion batteries. *J. Solid State Electrochem.* **2012**, *16*, 819−824.

(55) Silversmit, G.; Depla, D.; Poelman, H.; Marin, G. B.; Gryse, R. D. Determination of the V2p XPS binding energies for different vanadium oxidation states (V5+ to V0+). *J. Electron Spectrosc. Relat. Phenom.* **2004**, *135*, 167−175.

(56) Johannes, M. D.; Hoang, K.; Allen, J. L.; Gaskell, K. Hole polaron formation and migration and migration in olivine phosphate materials. *Phys. Rev. B: Condens. Matter Mater. Phys.* **2012**, *85*, 115106.

(57) Piper, L. F. J.; Quackenbush, N. F.; Sallis, S.; Scanlon, D. O.; Watson, G. W.; Nam, K.-W.; Yang, X.-Q.; Smith, K. E.; Omenya, F.; Chernova, N. A.; Whittingham, M. S. Elucidating the nature of pseudo Jahn-Teller distortions in Li_xMnPO_4: Combining density functional theory with soft and hard x-ray spectroscopy. *J. Phys. Chem. C* **2013**, *117*, 10383−10396.

(58) Scofield, J. H. Theoretical Photoionization Cross Sections from 1 to 1500 keV. Lawrence Livermore National Laboratory Rep. UCRL-51326, Lawrence Livermore National Laboratory: Livermore, CA, 1973.

(59) Liu, L.; Henrich, V. E.; Ellis, W. P.; Shindo, I. Bulk and surface electronic structure of Li_2O. *Phys. Rev. B: Condens. Matter Mater. Phys.* **1996**, *54*, 2236−2239.

(60) Ensling, D.; Thissen, A.; Jaegermann, W. On the formation of lithium oxides and carbonates on Li metal electrodes in comparison to LiCoO2 surface phases investigated by photoelectron spectroscopy. *Appl. Surf. Sci.* **2008**, *255*, 2517−2523.

(61) Goodenough, J. B.; Kim, Y. Locating redox couples in the layered sulfides with application to Cu[Cr2]S4. *J. Solid State Chem.* **2009**, *182*, 2904−2911.